Long-range oxygen ordering linked to topotactic oxygen release in Pr2NiO4+δ fuel cell cathode material

Rajesh Dutta, Avishek Maity, Anna Marsicano, Monica Ceretti, Dmitry Chernyshov, Alexei Bosak, Antoine Villesuzanne, Georg Roth, Giuditta Perversi, Werner Paulus

Long-range oxygen ordering linked to topotactic oxygen release in $Pr_2NiO_{4+\delta}$ fuel cell cathode material

Rajesh Dutta[a,b,‖], Avishek Maity[a,¥], Anna Marsicano[a], Monica Ceretti[a], Dmitry Chernyshov[c], Alexeï Bosak[d], Antoine Villesuzanne[b], Georg Roth[e], Giuditta Perversi[a,&], Werner Paulus[a]*

[a.] *ICGM, Université de Montpellier, CNRS, ENSCM, Montpellier, France. E-mail : werner.paulus@umontpellier.fr*
[b.] *CNRS, Univ. Bordeaux, Bordeaux INP, ICMCB, UMR 5026, F-33600 Pessac, France*
[c.] *Swiss-Norwegian Beam Lines at European Synchrotron Radiation Facility, 71 avenue des Martyrs, 38000 Grenoble.*
[d.] *European Synchrotron Radiation Facility, 71 avenue des Martyrs, 38000 Grenoble, France*
[e.] *Institut für Kristallographie, RWTH Aachen, Jägerstrasse 17-19, 52056 Aachen, Germany*
Present Addresses:
[‖]Institut für Kristallographie, RWTH Aachen, Jägerstrasse 17-19, 52056 Aachen, Germany, Outstation at Heinz Maier-Leibnitz Zentrum, FRMII, Lichtenbergstrasse 1, D - 85747 Garching, Germany
[¥] Heinz Maier-Leibnitz Zentrum, FRM-II, TUM, Lichtenbergstrasse 1, 85748 Garching, Germany
[&]Maastricht University, Kapoenstraat 2, 6211 KW Maastricht, The Netherlands.
R. Dutta, A. Maity and A. Marsicano contributed equally to this work
Electronic Supplementary Information (ESI) available: Figures S1-S7 and table S1.

Abstract:

Solid oxide ion conductors are technologically important for oxygen membranes, sensors and solid oxide fuel cells (SOFC). However, oxygen diffusion is a thermally activated process, and materials operating at ambient temperature are rare, as related diffusion mechanisms are poorly understood. We report here on a hidden spontaneous oxygen release reaction that interconvert two stoichiometric phases of the SOFC material $Pr_2NiO_{4+\delta}$ with unprecedented structural complexity at ambient temperature. A slight change in the oxygen stoichiometry from δ = 0.25 to δ = 0.225 involves a transition between two competing modulated superstructures, showing long-range translational periodicities up to 94 Å. Our findings demonstrate correlated oxygen diffusion within the bulk phase at room temperature, which is accompanied by the formation of long-range modulated superstructures up to the lower mesoscale. Large-scale ordered structures found here for $Pr_2NiO_{4+\delta}$ are rather indicative of non-local interactions and interpreted here to be mediated via structural deformations. This unexpected behavior is discussed in terms of an unconventional understanding of low-T oxygen diffusion mechanisms and its potential to conceive and optimize oxygen ion conductors, which are an important class of compounds relevant to technological applications.

Introduction

Oxygen diffusion mechanisms in solid oxides are of importance for many technological applications such as electrochemical energy conversion devices or air separation membranes.[1-4] In this regard non-stoichiometric transition metal oxides are of particular interest, as they can take up and release oxygen in stoichiometric quantities in a reversible topotactic reaction, down to very moderate temperatures. As a phenomenon, oxygen ion mobility at moderate temperatures is already surprising by itself, considering its twofold negative charge and diameter of 2.8 Å. Three decades ago, an enhanced oxygen mobility in Brownmillerite type solid electrolytes at moderate temperatures (c.a. 400 °C) was perceived as pivotal progress, as they turned out to be surprisingly competitive, compared to stabilized zirconia at 800 °C.[5]

Unusually high oxygen mobility at room temperature, with a diffusion coefficient of $1.4\times10^{-11}cm^2/s$, was, however, reported almost 5 decades ago following electrochemical studies on $Nd_{1-x}Sr_xCoO_{3-\delta}$.[6] Despite this spectacular result, no follow-up of these findings was reported. That tremendously changed [7-9] with the discovery of superconductivity in electrochemically oxidized $La_2CuO_{4.07}$, showing a T_C of ≈ 44 K.[10] Meanwhile, oxygen diffusion at ambient temperature was demonstrated to exist for a few more transition metal oxides with brownmillerite/perovskite/Ruddlesden-Popper-type frameworks, showing reversible chemical or electrochemical oxygen intercalation at ambient conditions, while the underlying diffusion mechanism itself remains unclear so far.[11-14] Further on, *local oxygen ordering* at room temperature has been discussed to take place on a local level, as indirectly concluded for oxygen deficient $YBa_2Cu_3O_{7-x}$, as obtained by quenching from high temperatures.[15, 16] The only case reported so far for a spontaneous topotactic oxidation at room temperature is La_2CoO_4.[17, 18] More recently, room temperature oxygen mobility without applying any (electro)-chemical potential, has been evidenced for $Nd_2NiO_{4+\delta}$ by *ab initio* molecular dynamics calculations combined with inelastic neutron scattering experiments.[19, 20]

Ruddlesden-Popper phases, e.g. $La_2MO_{4+\delta}$ (M= Cu, Ni, Co) and $(Pr/Nd)_2NiO_{4+\delta}$, constitute in this context a special case; in particular, $Pr_2NiO_{4+\delta}$ became a prominent example, combining high oxygen diffusion rates together with a performant catalytic activity.[7, 10, 11, 21-28] $Pr_2NiO_{4+\delta}$ is regarded as one of the most promising oxygen membranes already at moderate temperatures, i.e. in a temperature range around and below 400 °C. [4] It can further intercalate reversibly oxygen ions via electrochemical red/ox reactions at room temperature.[7] Its crystal structure can be seen as a stacking of rigid NiO_2-layers, interlaced by Pr_2O_2 rock salt units, which can host interstitial oxygen atoms (O_{int}).[29, 30] The presence of interstitial oxygen atoms has been shown by single crystal neutron diffraction to be decisive to enable low-T oxygen diffusion, as they induce strongly anharmonic displacements of all apical oxygen (O_{ap}) and praseodymium atoms inside the Pr_2O_2 layers, thus creating a shallow 1D oxygen diffusion pathway between apical and interstitial oxygen sites.[4, 26] Thereby complex oxygen ordering has been reported for several Ruddlesden-Popper type oxides at higher doping levels.[12, 27, 31]

Here we report on room temperature oxygen diffusion in $Pr_2NiO_{4+\delta}$ as evidenced by mass, composition, and structural changes. Single crystal synchrotron diffraction uncovered a complex oxygen ordering at room temperature for as-grown $Pr_2NiO_{4.25}$. Leaving $Pr_2NiO_{4.25}$ at ambient conditions, leads to a release of a small amount of oxygen on a timescale of several months, yielding $Pr_2NiO_{4.225}$ as the equilibrium phase at ambient conditions. We evidenced that this topotactic release reaction results to the formation of a well-defined 3D-incommensurate oxygen ordering of

unprecedented complexity, unveiling unequivocally room temperature oxygen diffusion as a bulk property.

Long-range oxygen ordering was found to be stable up to 365 °C, i.e. the phase transition into the tetragonal high-T phase. This transition is accompanied by the onset of $^{18}O/^{16}O$ isotope exchange reaction in $Pr_2Ni^{18}O_{4.25}$, together with the formation of anisotropic structured diffuse scattering. Differences in the oxygen diffusion mechanisms below and above the phase transition are discussed for the different ordering schemes of interstitial oxygen atoms. Our findings call for new theoretical concepts and experimental studies to better understand oxygen diffusion mechanisms on a microscopic scale.

Experimental

Single crystal growth. Single crystals of $Pr_2NiO_{4.25}$ of about 6 mm diameter and 10 cm long have been grown by the floating zone method at ICGM as described previously.[27] Crystals of $50 \times 50 \times 200$ μm^3 size, suitable for synchrotron diffraction experiments, have been dressed to size by sanding a crystal piece, which was cut from the as-grown crystal. The needles have been then glued with the long axis parallel to the quartz tubes, used as sample holders.

Synchrotron and X-ray diffraction experiments. Several beamlines at the ESRF have been used for diffraction experiments as outlined in the text. For all experiments the needle shaped crystals have been turned around their long axis (360° in steps of 0.1°/image), in order to minimize absorption and extinction problems. Typical exposure times were 0.1-0.3 s/frame on all synchrotron beamlines, while 60s/frame were used for the Stoe STADIVARI laboratory diffractometer ($MoK_{\alpha1,2}$, Xenocs Microfocus tube, Pilatus 200K). The following wavelengths, primary monochromators and detectors have been used: ID23: 0.688801 Å, Si(111), Pilatus 6M. ID29: 0.7 Å, Si(111), Pilatus 6M ; BM01A: 0.6630 Å, Si(111), Pilatus 2M Detector, PANalytical X'Pert powder diffractometer (Cu $K_{\alpha1,2}$) equipped with an X'Celerator detector. More experimental details are given in Table S1.

Thermogravimetric studies. TG measurements were carried out in 33%O_2/67%Ar atmosphere on a Perkin Elmer TG8000 (mass accuracy 0.1μg). Heating/cooling rates were 5K/min. A baseline correction with an empty sample holder was applied to all measurements.

Data Analysis. Single crystal data analysis has been performed using the SNBL Tool Box[32], the Crysalis blue (Rigaku) and ALBULA software package (Dectris) as well as the X-Area software package (STOE Darmstadt).

Results

Basic structure and twinning phenomena

The structure of $Pr_2NiO_{4+\delta}$ is schematically shown in Figure 1a; the extra oxygen is accommodated in interstitial sites in the Pr_2O_2 rock salt layer, thus being coordinated by 4 Pr and 4 O_{ap} atoms, both forming a tetrahedron. As-grown $Pr_2NiO_{4.25}$ is generally reported to adopt an orthorhombic symmetry with *Fmmm* space group. However, its true symmetry at ambient temperature is monoclinic with a subtle deviation from the orthorhombic symmetry, adopting the space group *F112/m* (Figure *S1*). The symmetry lowering towards the monoclinic system thereby triggers the formation of a complex twin

domain structure with up to 16 monoclinic twin individuals by pseudo merohedry, as illustrated in Figures *1b* and *S2*.

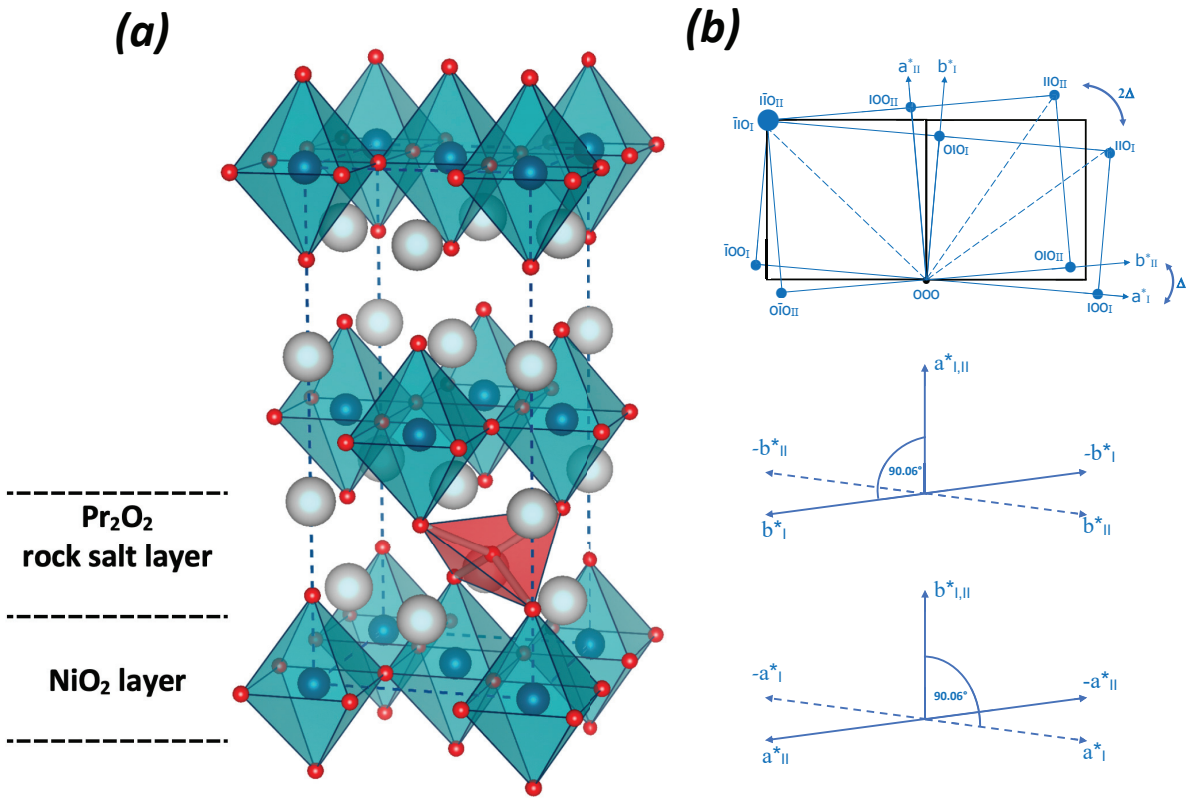

Figure 1: (a): *Structure and twin-domain structure of $Pr_2NiO_{4.25}$ (blue: Ni, red: O, grey: Pr). Interstitial oxygen atoms are located in the Pr_2O_2 rock salt layer, tetrahedrally coordinated by the apical oxygen as well as Pr atoms. Here only one out of 8 equivalent O_{int} positions is shown, the average occupation being 1/8.* ***(b):*** *Twinning scheme showing tetragonal (top black), orthorhombic and monoclinic twin domains, the latter related by [100] and [010], i.e. by rotation around the a* or b*-axis, respectively (see Figure S2 for more details).*

Room temperature diffusion: two modulated structures of $Pr_2NiO_{4.25}$ and $Pr_2NiO_{4.225}$

Reciprocal space mapping of the as-grown $Pr_2NiO_{4.25}$ single crystal is shown in Figure 2 for the reconstructed *(hk0)*- and *(hk1)*-planes, obtained on ID23@*ESRF*. The presence of a remarkable number of superstructure reflections becomes evident, their intensities being around 3-5 orders of magnitude weaker with respect to the basic reflections. This complicated diffraction pattern can be rationalized in terms of a modulation of a basic twinned, monoclinic structure (see Figure 3 and S2). The indexing of all incommensurate superstructure reflections becomes possible, assuming an incommensurate modulation vector $\boldsymbol{Q}_n = \alpha_n\boldsymbol{a}^* + \beta_n\boldsymbol{b}^* + \gamma_n\boldsymbol{c}^*$ added to the position of each Bragg reflection $\boldsymbol{G} = h\boldsymbol{a}^* + k\boldsymbol{b}^* + l\boldsymbol{c}^* + m_n\boldsymbol{Q}_n$, with m_n being an integer, indicating the order of the corresponding satellite reflections.[31, 33, 34] The underlying modulation vector, found for as-grown $Pr_2NiO_{4.25}$ crystals, corresponds to a commensurate description with $\boldsymbol{Q}_n = \pm 7/9\boldsymbol{a}^* + 5/9\boldsymbol{b}^*$.

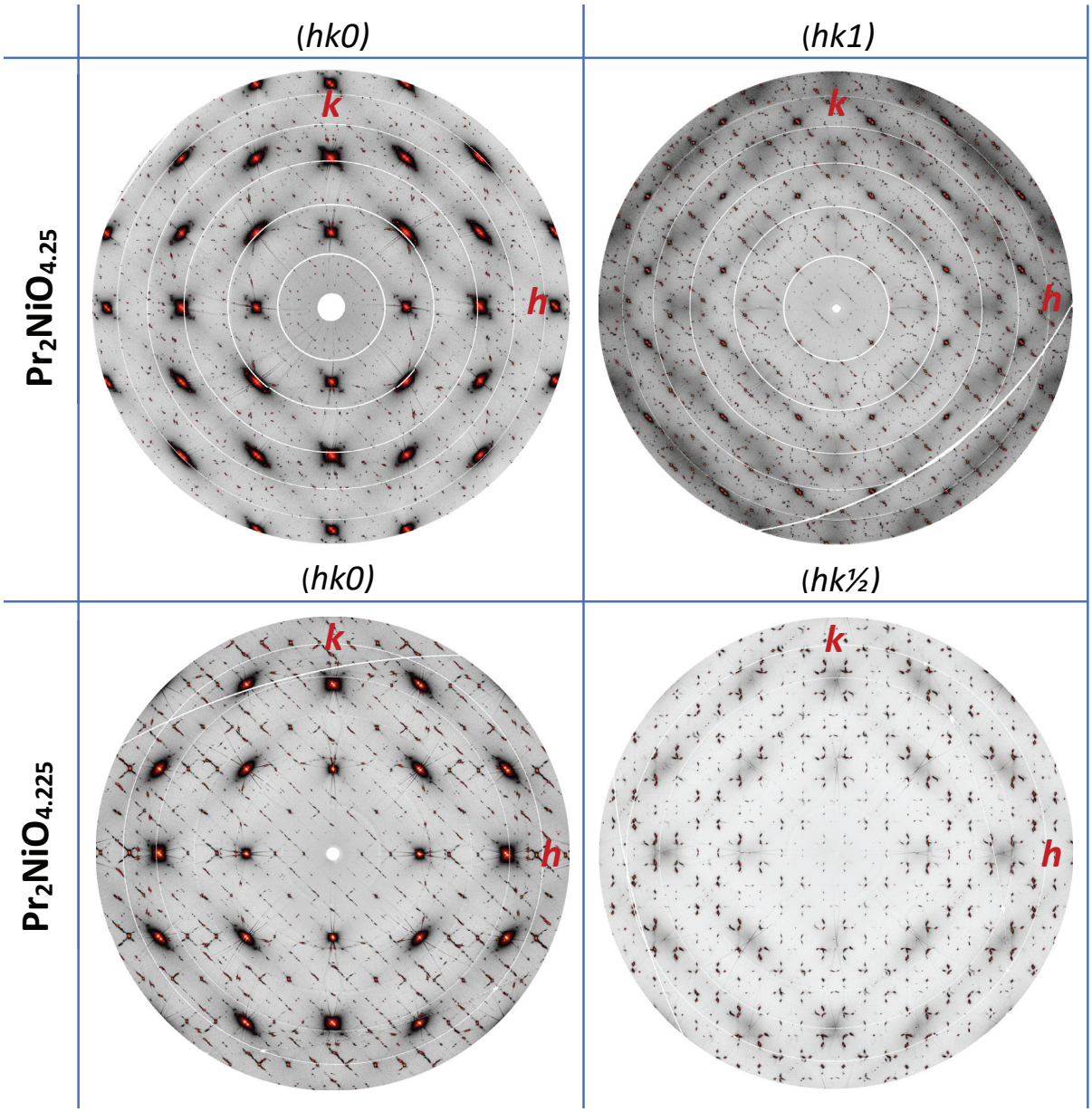

Figure 2: *Reciprocal layers for as-grown $Pr_2NiO_{4.25}$ and $Pr_2NiO_{4.225}$, reconstructed from diffraction data obtained on ID23@ESRF (top) and ID29@ESRF (bottom) at RT. Large spots surrounded by diffuse scattering correspond to reflections of the basic structure, while the small spots are superstructure reflections. The corresponding vector schemes for indexation of different domains are given in Figure 3, resulting into a commensurate modulation vector of $Q_n = \pm 7/9a^* + 5/9b^*$ and $Q_n = \pm 5/6a^* + 1/2b^*$ respectively for both phases. The monoclinic symmetry yields for both cases a complex overlay of 8 twin domains as outlined in Figure 1b and S2.*

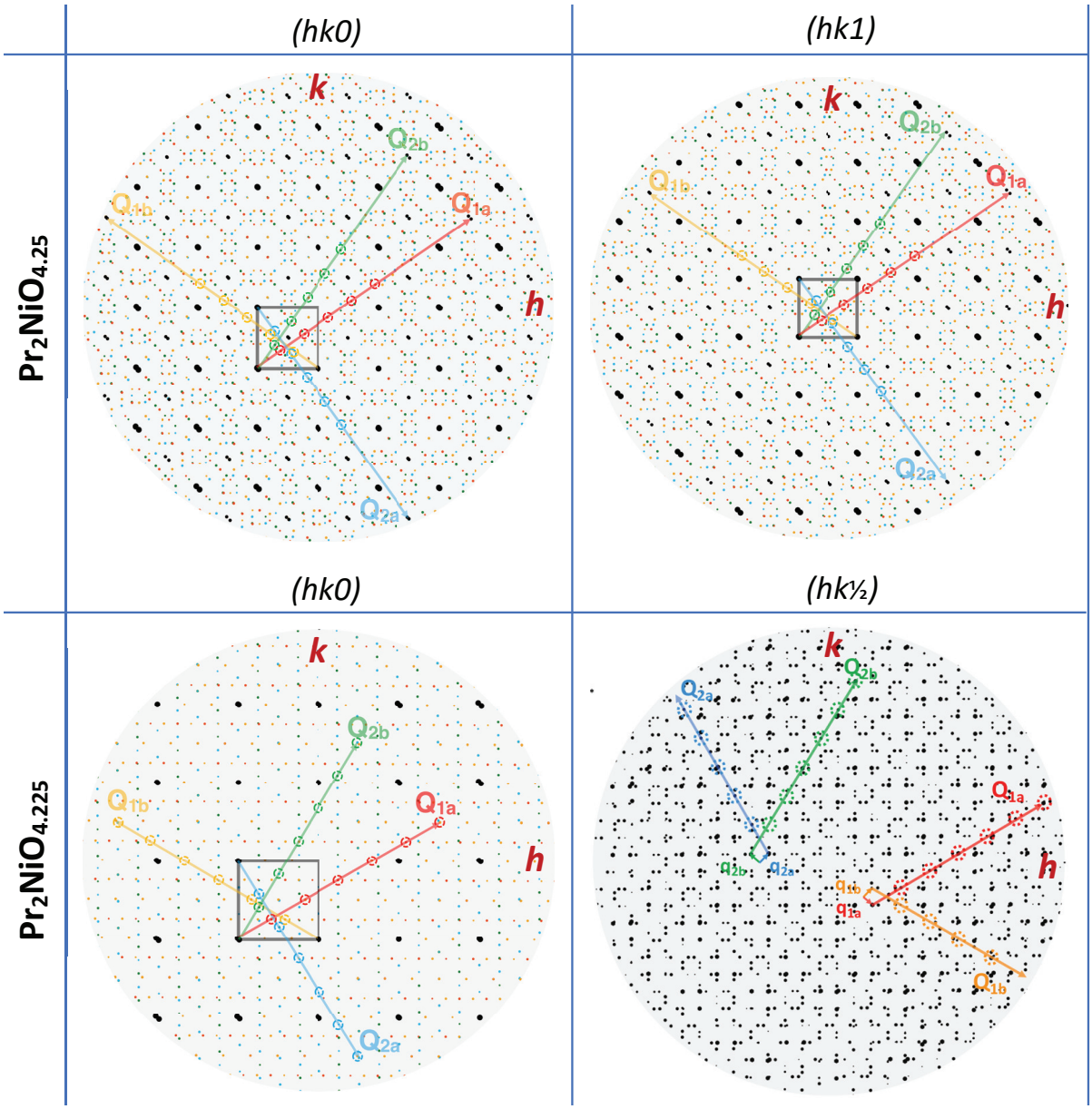

Figure 3: *Vector scheme of the reciprocal layers for $Pr_2NiO_{4.25}$ (top) and $Pr_2NiO_{4.225}$ (bottom) as presented in Figure 2.* ***Top:*** *For $Pr_2NiO_{4.25}$ the simulated reconstructions, only 4 of the 8 possible commensurate modulation vectors of $\mathbf{Q_n} = \pm 7/9\mathbf{a}^* + 5/9\mathbf{b}^*$ are outlined for simplicity, taking into account up to 5th order satellite reflections and monoclinic twin domains around [010] only for the two orthorhombic twin individuals. The other four modulation vectors taking into account twin domains around [100] virtually yield identical satellite positions, related to the small angular separation of twin domains by 0.06° only. Spots in different colors refer to different monoclinic domains. Large black spots correspond to basic reflections with F-centering, small black spots indicate a violation for F-centering.* ***Bottom:*** *The corresponding indexing for $Pr_2NiO_{4.225}$ again with a "commensurate" modulation vector of $\mathbf{Q_n} = \pm 5/6\mathbf{a}^* + 1/2\mathbf{b}^*$. We note that the (hk½)-plane doesn't show significant intensities for the as grown $Pr_2NiO_{4.25}$ phase, but develops significant intensities with the topotactic oxygen release (see also Figure S5), indicating the formation of a 3D long-range oxygen ordering proceeding at room temperature, which can be described using the (3+2) superspace formalism.*

A simulation for possible satellite reflection positions in the superspace group F112/m(αß0)(00), (a subgroup of the standard setting C2/m), with the c-axis as the monoclinic axis, is shown in Figure 3. It takes into account the peak splitting of the orthorhombic twin domains together with the twinning by pseudo-merohedry for the monoclinic twin individuals. The small deviation of the monoclinic angle (90.03°) virtually superimposes the satellite reflections of the different monoclinic twin individuals, which cannot be spatially discerned even in high-resolution single crystal synchrotron data. As a consequence, overlaying reflection pairs e.g. (hkl) and $(h\bar{k}\bar{l})$ as well as (hkl) and $(\bar{h}k\bar{l})$ (outlined in Figure 1b and commented under Figure S2), emerge to be no longer equivalent in a monoclinic symmetry, which consequently does no longer allow collecting individual satellite intensities, i.e. structure factors, mandatory for structure solving methods.

As it can be seen in Figure 3 and 4, the commensurate modulation vector leads principally to an indexation scheme, allowing up to 9th order satellite reflections, while we observed the absence of satellites beyond 5th order. On top of the basic reflections of the underlying *F*-centered lattice, we also observed low intensity reflections, fulfilling the conditions of (*h+k*), (*h+l*) and (*k+l*) all odd. They show a small but significant deviation from F-centering, rendering the true lattice translation to be primitive and the space group of the modulated structure becoming *P112/m(αß0)(00)*. These P-type reflections show, however, a more complex scenario, as they are systematically overlaid with scattering contributions originating from diffuse rods along the c-axis (see Figure S3), which might be attributed to disorder in the (a,b)-plane and/or a specific domain structure of the crystal.

As further outlined below, the reinvestigation of the as-grown $Pr_2NiO_{4.25}$ single crystals after several months revealed changes not only of the modulation period of the satellite reflections, but also of small but significant changes in the oxygen stoichiometry. From systematic thermogravimetric studies, we were able to evidence that freshly prepared $Pr_2NiO_{4.25}$ releases oxygen on a timescale of several days or months at ambient conditions, yielding $Pr_2NiO_{4.225}$ as the final reaction product. The kinetics of this topotactic oxygen release process strongly depends on the grain size. Although the relative weight change between $Pr_2NiO_{4.225}$ and $Pr_2NiO_{4.25}$ is barely 0.1%, we could unambiguously confirm these variations in the oxygen stoichiometry by thermogravimetric analysis (TGA), in a reproducible way.

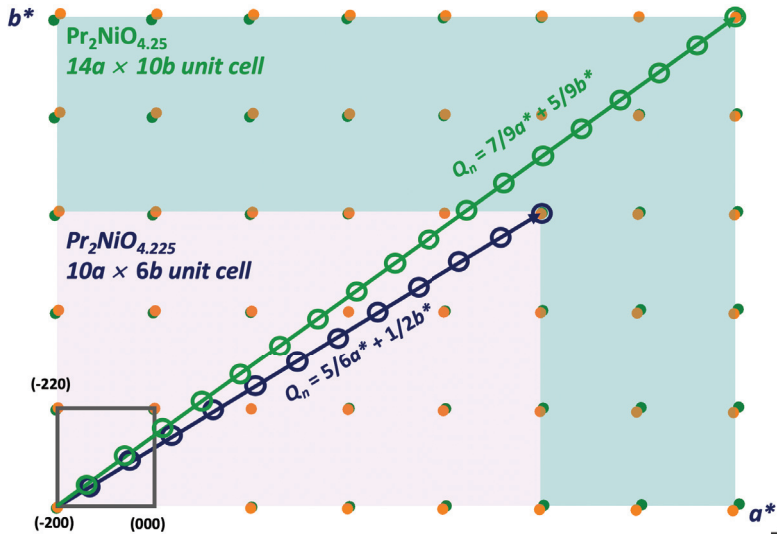

Figure 4: *Scheme of the structural changes for $Pr_2NiO_{4.25}$ and $Pr_2NiO_{4.225}$, both showing a commensurate indexation. One average F- unit cell and corresponding satellite reflections for both phases are outlined.*

On an absolute scale the oxygen stoichiometry is, however, much more difficult to evaluate. Taking into account the discussions of the extra oxygen stoichiometry in Refs [19, 20, 35] and especially the argument that local distortions of the apical oxygen atoms, induced by the presence of interstitial oxygen atoms, are sterically limiting the maximum extra oxygen stoichiometry to $\delta = 0.25$, we fixed the highest oxygen content from the TGA experiments at 100.1% (see Figure 5a) to nominally correspond to $Pr_2NiO_{4.25}$. Based on this, the starting phase complies with a stoichiometry of $Pr_2NiO_{4.225}$, which is in good agreement with stoichiometries reported elsewhere.[7, 27] The oxygen release of $Pr_2NiO_{4.25}$ is found to be fully reversible, as $Pr_2NiO_{4.225}$ gets fully re-oxidized upon heating in an O_2-containing atmosphere above 300 °C. During the cooling process, $Pr_2NiO_{4.25}$ is formed around 300 °C, and all interstitial oxygen atoms stay trapped inside, even on cooling to room temperature. The reason for the slow oxygen release of O_{int} is probably related to the kinetic stability of the oxygen-rich phase, brought upon by a decrease of the average Ni-O_{ap} distance and consequently reducing the bond-length mismatch between Pr and the O_{ap}, as further discussed in [26]. $Pr_2NiO_{4.225}$, obtained via oxygen release from $Pr_2NiO_{4.25}$, shows a different arrangement of the satellite reflections, as compared to the as-grown crystal (Figure 2). The related diffraction pattern can again be rationalized in a similar way as discussed for $Pr_2NiO_{4.25}$. It is constituted of 4 overlaid monoclinic twin domains per orthorhombic twin individual, showing a monoclinic modulated structure (Figure 3) with a commensurate oxygen ordering modulation vector $\boldsymbol{Q_n = \pm 5/6 a^* + 1/2 b^*}$, involving satellite reflections of up to 5th order (see Figures 3 and S2, S4, S5). Beside the changes in the modulation vector, the topotactic oxygen release goes along with additional satellite reflections, having no correspondence to the as grown $Pr_2NiO_{4.25}$ phase. This involves the generation of new diffraction planes with half integral values, e.g. the *(hk½)*-plane as illustrated in Figure S3. All satellite reflections on the (***a**-b****)-plane irrespective of *l* can be indexed in a *(3+2)*-dimensional superspace with a general vector $\boldsymbol{G = ha^* + kb^* + lc^* + m_1Q_n + m_2q_n}$ with $0 \leq |m_1| \leq 6$ and $0 \leq |m_2| \leq 1$, while *n* symbolizes the number of the twin individual, $1 \leq n \leq 4$. With $\boldsymbol{q_n}$ = ±0.25**a*** + 0.25**b*** + 0.5**c***, the *(3+2)* superspace group is *P112/m(α$_1$ß$_1$0)(0s)(α$_2$ß$_2$1/2)(00)*. This clearly underlines the genuine 3D incommensurate character of the long-range oxygen ordering induced by the topotactic oxygen release at room temperature.

Despite the differences in the diffraction patterns, we note that for both phases all superstructure reflections are sharp and well-defined up to high diffraction angles, which directly evidences an extremely well-established long-range oxygen order implying a homogenous distribution, co-existing with a slow oxygen diffusion rate. In this sense room temperature oxygen mobility might be understood a prerequisite for long-range oxygen ordering generally.

We also note the existence of additional reflections in the (hk0)-planes of both, $Pr_2NiO_{4.25}$ and $Pr_2NiO_{4.225,}$ related to the epitaxial growth of NiO, which existence has been reported before segregation but not as an intergrowth. 4 distinct twin domains have been identified which turned out to be twinned around [110], as further discussed in Fig. S6 and which are stable with temperature. Interestingly we could further on observe additional smaller spots at higher *d*-values, which correspond by their scattering angle and orientation to Ni_3O_4, a spinel phase for which lattice parameter of a = 8.20 Å has been proposed. This phase has so far only been reported following irradiation damage of NiO as given in [36, 37]. Ni_3O_4 is epitaxially grown on $Pr_2NiO_{4+\delta}$ with $[100]_{Ni3O4}$ parallel to the $[110]_{PNO}$, most probably due to their similar *d*-values: $d_{(200)}Ni_3O_4$ = 4.1 Å, $d_{(220)}$PNO = 3.88Å, resulting into a lattice mismatch of about 5%.

Phase transition phenomena and fast $^{18}O/^{16}O$ isotope exchange regime

$Pr_2NiO_{4.25}$ undergoes an order-disorder phase transition at 365 °C, related to the melting of the oxygen ordering superstructure, while changing the symmetry from monoclinic to tetragonal [26]. The phase transition coincides with an onset of enhanced oxygen diffusion, as evidenced by *$^{18}O/^{16}O$* isotope exchange experiments (Figure 5b). This experiment was carried out on heating polycrystalline $Pr_2Ni^{18}O_{4.25}$ in a 33% O_2 / 67% Ar atmosphere, while the *$^{18}O/^{16}O$* exchange is directly indicated by the respective mass loss. In this context, it is remarkable that single crystals of about 2 x 2 x 2 mm^3 volume reveal oxygen isotope exchange kinetics which are almost comparable to µm-sized powder samples. Quantitative *$^{18}O/^{16}O$* bulk exchange is thus proceeding in less than 40 min. under dynamical heating conditions above 300 °C.

Strong structural correlations are confirmed to persist above the phase transition, revealed by the appearance of diffuse scattering around the former satellite positions throughout the tetragonal phase (Figure 5). These structural changes directly indicate short-range correlations of interstitial oxygens at high temperatures, i.e. in the fast diffusion regime. The *correlation range*, as obtained from the inverse of the FWHM of the diffuse scattering (see Figure S7), has been determined to be around 25 Å. The butterfly-shaped diffuse scattering near Bragg reflections, already present at room temperature (Figure 2) is anisotropic, as expected from elastic properties on a tetragonal symmetry (Figure 6b). It is worth noting that lobes of the diffuse scattering point towards the [110]-direction, directly matching with the oxygen diffusion pathway inside the Pr_2O_2 rock salt plane, as evidenced from single crystal neutron diffraction studies at 400 °C via a continuous overlap of the nuclear density distribution between apical and interstitial oxygen sites. [26]

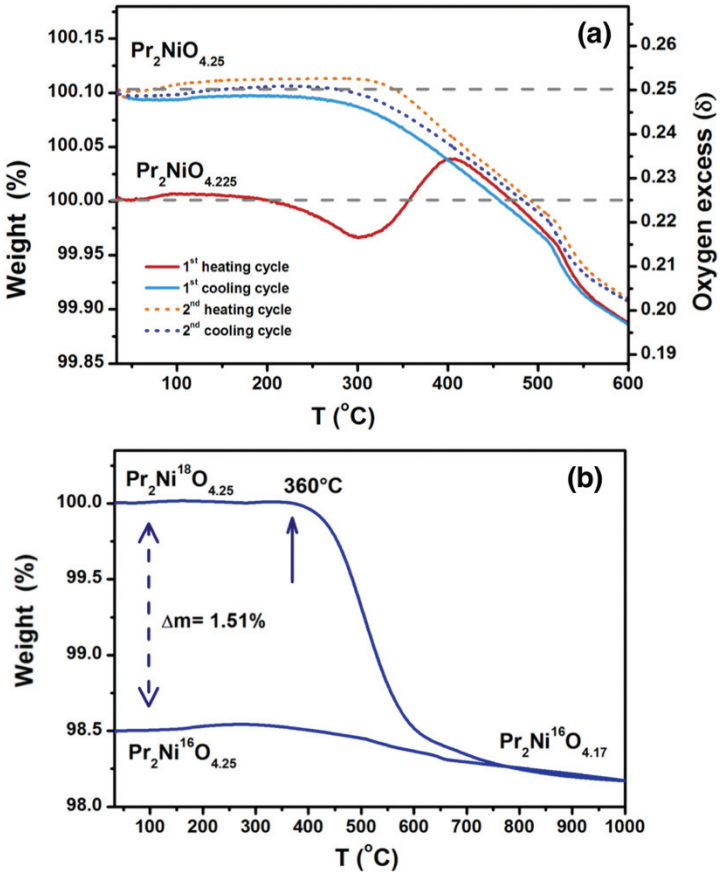

***Figure 5**: Thermogravimetric study of (a) Pr2Ni16O4.225 and (b) Pr2Ni18O4.25, carried out in an atmosphere of 33%O2/67%Ar with a heating/cooling rate of 5 °C/min. **(a):** Polycrystalline Pr2Ni16O4.225 first starts to take up oxygen at around 300 °C (red continuous line); upon cooling from 600 °C (light blue continuous line), oxygen uptake towards Pr2NiO4.25 occurs down to 300 °C, and remaining constant down to room temperature. A second heating/cooling cycle (dotted orange/blue lines) reversibly follows the 1st cooling cycle. **(b):** Weight loss observed for Pr2Ni18O4.25 (≈ 70% 18O enrichment) related to 18O/16O oxygen isotope exchange towards Pr2Ni16O4.17 at 1000 °C, yielding Pr2Ni16O4.25 after cooling to room temperature. Unhindered 18O/16O exchange, i.e. oxygen mobility, sets in above 360 °C, which is close to the monoclinic/tetragonal phase transition at 365 °C.*

On cooling to ambient temperature, sharp satellite reflections start to appear around 400 °C, in co-existence with a strong diffuse scattering intensity. The condensation of all satellite reflections upon cooling is completed at 350 °C (Figure 6d); the commensurate modulation vector of the as formed satellite reflections $\boldsymbol{Q_n = \pm\, 7/9a^* + 5/9b^*}$ remains invariant from 350 °C down to ambient.

Discussion

Room temperature oxygen diffusion was unequivocally evidenced as a bulk property for $Pr_2NiO_{4+\delta}$, combining single crystal diffraction experiments together with precise TGA measurements. The diffusion goes along with a topotactic oxygen release and co-exists with long-range oxygen ordering.

Hereby the seemingly unconstrained transition involving two commensurately ordered phases comply with an apparent structural sensitivity to already minor changes in the oxygen stoichiometry, i.e. $\Delta\delta$ = 0.025. The different ordering schemes thus dispose of defined and energetically close-lying minima in the energy landscape, while the room temperature oxygen diffusion is apparently not perturbing the long-range oxygen ordering.

The observed translational periodicity for oxygen ordering, as follows from the modulation vectors, resulting for the (*14a* $\times$ *10b)*-unit cell in 94 Å. This periodicity may be compared with typical unit cell dimensions in supramolecular compounds; however, the underlying interactions are quite different. A complex self-organization of molecular assemblies is essentially achieved on the basis of weak and non-covalent local interactions between distinct molecules. Large-scale ordered structures found here for $Pr_2NiO_{4+\delta}$ are rather indicative of non-local interactions between interstitial and apical oxygen atoms and presumably mediated via structural deformations, e.g. a well-defined octahedra tilting pattern throughout the whole layered structure associated with the rearrangement of the interstitial atoms.

Further complexity may also arise from electronic ordering, e.g. charge ordering of Ni^{2+}/Ni^{3+}. Such type of ordering is, however, supposed to appear at lower temperatures notably below 100 K. The superstructure reflections observed are thus expected to originate from oxygen ordering.

On heating to moderate temperatures, the system enters into a fast diffusion regime around 360 °C, as qualitatively indicated by $^{18}O/^{16}O$ isotope exchange reactions. At the same temperature, long-range ordering is substituted by short-range structural correlations of interstitial oxygens, revealed by the appearance of diffuse scattering. The distribution of diffuse scattering intensity in reciprocal space resembles the superstructure reflections observed at room temperature, that reversibly reappear upon cooling. The diffuse scattering signifies a short-range ordering of the interstitial oxygens co-existing with the fast oxygen diffusion with a *correlation range* of about 25 Å.

These findings critically question the view of oxygen diffusion as a local process with either single particle-type diffusing species or push-pull O_{int}-O_{ap} events; they rather suggest a correlated, cooperative character of the migration of the interstitial oxygen atoms at least in the sense of time-averaged local structures. These correlations may be mediated by the same structural distortions that led to long-range ordering at lower temperatures. The important difference between the two diffusion

regimes lies in their respective time scale. At room temperature the kinetics of the oxygen diffusion is substantially slower than that for long-range ordering processes. In case of the HT phase, oxygen diffusion is certainly faster than the formation of long-range ordering, but still not fully uncorrelated as indicated by the presence of significant diffuse scattering. The simultaneous appearance of high oxygen mobility and diffuse scattering resembling superstructure reflections indicates a certain cooperativity for the diffusion process. The (re-)organization of interstitial oxygen atoms thus requires a sufficiently *flexible* oxide matrix and linked *dynamics*. Simultaneous perturbations of the electronic structure, vibrational properties and elastic distortions, that accompany gradient-driven migration of the interstitial oxygen may serve to mediate the observed structural correlations conjugated with the diffusion process. Oxygen diffusion as encountered here, thus resembles to a polaron-type mobility that implies that the diffusion event is accompanied by a significant deformation of the lattice, as observed in [38-41].

In this context structural phase transitions in Ruddlesden-Popper type frameworks induce structural instabilities of the apical oxygen atoms, creating correlated displacements from their equilibrium positions. Together with the presence of interstitial oxygen atoms, those displacements provide a shallow oxygen diffusion pathway between apical and interstitial sites.[3, 4, 19-23, 26, 35] A collective/correlated character of the diffusion process also agrees with a phonon-assisted diffusion mechanism, considering phonons as collective excitations of the entire structure.[35, 42, 43] In this respect, the collective effects inherent to an ordered structure may enhance the diffusion rate, contrary to the expectation that any kind of ordering would hinder the mobility. It becomes also evident that, for lattice dynamics calculations to include such contributions to diffusion processes, very large simulation ranges are required, at least not smaller than the corresponding correlation length.

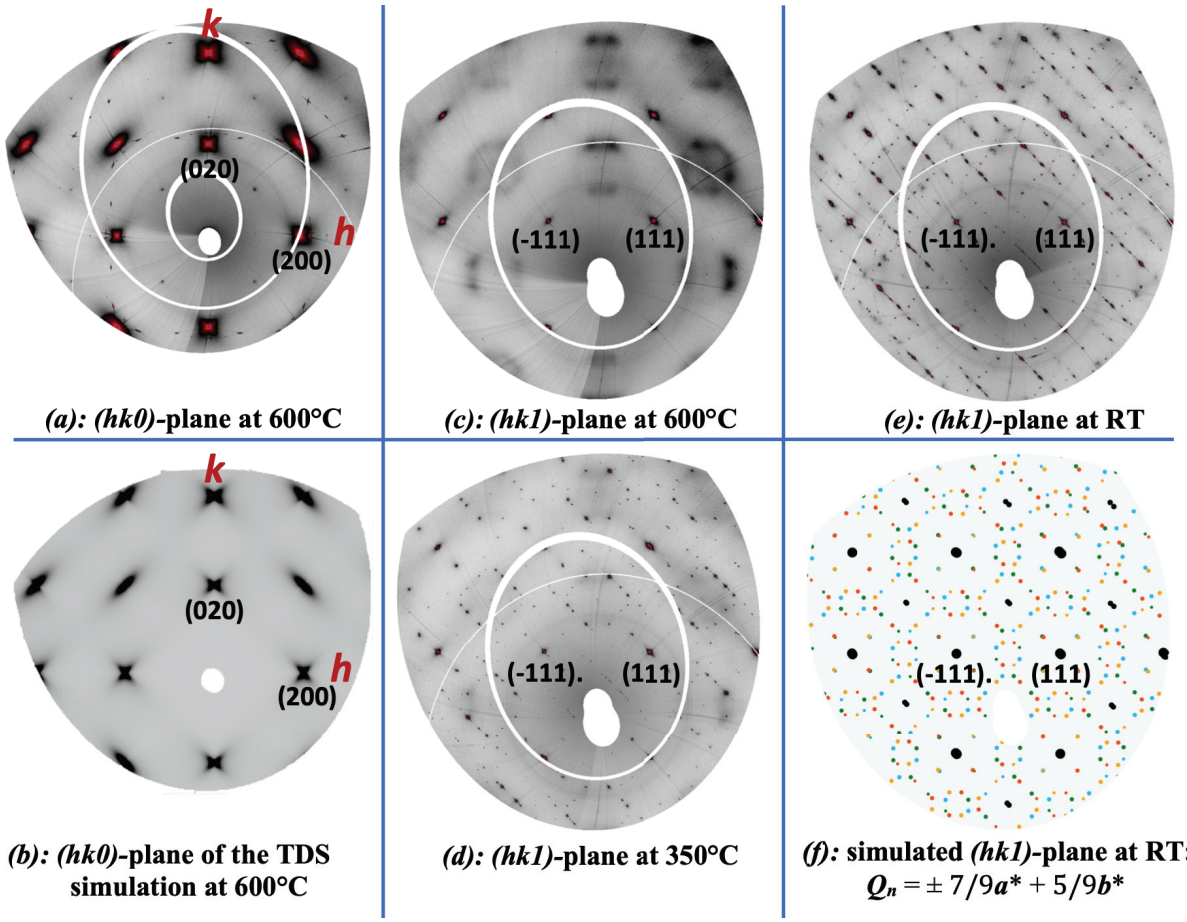

Figure 6: *Reconstructed diffraction planes of $Pr_2NiO_{4+\delta}$ at different temperatures, obtained on ID28@ESRF in air. The butterfly-shaped profiles in the (hk0)-layer in* ***(a)*** *are induced by the monoclinic/tetragonal phase transition and essentially based on TDS only* ***(b)****, cf ref. [44, 45]. The lobes pointing into the [110]-direction of the tetragonal F-cell, go along with the oxygen diffusion pathway connecting O_{ap} and O_{int} sites.[26] The extra spots in the (hk0)-plane at 600 °C correspond entirely to epitaxially intergrown NiO (cf Figure S7).* ***(c-e):*** *(hk1)-planes at different temperatures;* ***(f):*** *Simulated (hk1)-plane of $Pr_2NiO_{4.25}$ including satellite reflections up to 5th order and $\mathbf{Q_n} = \pm 7/9\mathbf{a}^* + 5/9\mathbf{b}^*$; different colors are related to the different four monoclinic twin domains, fat black dots represent basic F-reflections, small black dots the positions of P-type reflections.*

Conclusions

Single crystal synchrotron X-ray diffraction revealed long-range oxygen ordering of unprecedented complexity up to the lower mesoscale in the oxygen membrane material $Pr_2NiO_{4+\delta}$. Further on we evidenced an unexpected reorganization of the 3D modulated structure, following a topotactic oxygen release proceeding at ambient temperature. The combination of complex oxygen ordering together with low-T oxygen mobility indicates a diffusion mechanism with significant structural and dynamical correlations. Oxygen ion mobility in solid oxides, essentially based on the presence of structural instabilities and amplified via phonon softening, favorized by the creation of long-range superstructures, may thus offer a new concept to rationalize new oxygen ion conductors or electrolytes. It will equally contribute towards an unconventional understanding of low-T diffusion mechanisms.

We conclude with a note on experiments: the structural features presented here became possible to identify thanks to the advent of bright synchrotron radiation and large area pixel detectors with nearly

zero background. The recent developments for the precision of thermogravimetric instrumentation made possible the detection of tiny variations of the oxygen stoichiometry. The combination of both experimental tools was necessary for this study.

Conflicts of interest

There are no conflicts to declare.

Acknowledgements

The authors acknowledge the beam times used at beamline ID23, ID29, ID28 and the SNBL at the European Synchrotron Radiation Facility (ESRF, Grenoble) and the "Plateforme d'Analyse et de Caractérisation" of the ICG Montpellier.

Financial support from the French National Research Agency (ANR) through the projects "Assisted Mechanisms for Oxygen Ionic conduction in non-Stoichiometric oxides" (AMOXIS, No. ANR-14-CE05-0016-02) and "Structural induced Electronic Complexity controlled by low temperature Topotactic Reaction" (SECTOR No. ANR-14-CE36-0006-01) is gratefully acknowledged.

References

1. E. D. Wachsman and K. T. Lee, *Science*, 2011, **334**, 935-939.
2. E. Kendrick, J. Kendrick, K. S. Knight, M. S. Islam and P. R. Slater, *Nature Materials*, 2007, **6**, 871.
3. A. Chroneos, B. Yildiz, A. Tarancón, D. Parfitt and J. A. Kilner, *Energy & Environmental Science*, 2011, **4**, 2774-2789.
4. D. Parfitt, A. Kordatos, P. P. Filippatos and A. Chroneos, *Applied Physics Reviews*, 2017, **4**, 031305.
5. J. B. Goodenough and Y. S. Zhen, *MRS Proceedings*, 2011, **210**.
6. T. Kudo, H. Obayashi and T. Gejo, *J. Electrochem. Soc.*, 1975, **122**, 159-163.
7. M. Ceretti, O. Wahyudi, G. André, M. Meven, A. Villesuzanne and W. Paulus, *Inorg. Chem.*, 2018, **57**, 4657-4666.
8. J. T. Mefford, W. G. Hardin, S. Dai, K. P. Johnston and K. J. Stevenson, *Nature Materials*, 2014, **13**, 726-732.
9. H. Jeen, W. S. Choi, M. D. Biegalski, C. M. Folkman, I. C. Tung, D. D. Fong, J. W. Freeland, D. Shin, H. Ohta, M. F. Chisholm and H. N. Lee, *Nature Materials*, 2013, **12**, 1057-1063.
10. A. Wattiaux, J.-C. Park, J.-C. Grenier, M. Pouchard, C.R. Acad. Sci. Paris 1990, t. 310 (Série II), 1047 - 1052.
11. S. Bhavaraju, J. F. DiCarlo, D. P. Scarfe, I. Yazdi and A. J. Jacobson, *Chem. Mater.*, 1994, **6**, 2172-2176.
12. A. Maity, R. Dutta, B. Penkala, M. Ceretti, A. Letrouit-Lebranchu, D. Chernyshov, A. Perichon, A. Piovano, A. Bossak, M. Meven and W. Paulus, *J. Phys. D: Appl. Phys.*, 2015, **48**, 504004.
13. R. Le Toquin, W. Paulus, A. Cousson, C. Prestipino and C. Lamberti, *Journal of the American Chemical Society*, 2006, **128**, 13161-13174.
14. A. Nemudry, M. Weiss, I. Gainutdinov, V. Boldyrev and R. Schöllhorn, *Chem. Mater.*, 1998, **10**, 2403-2411.

15. J. D. Jorgensen, S. Pei, P. Lightfoor, H. Shi, A. P. Paulikas and B. W. Veal, *Physica C: Superconductivity*, 1990, **167**, 571-578.

16. H. Shaked, J. D. Jorgensen, B. A. Hunter, R. L. Hitterman, A. P. Paulikas and B. W. Veal, *Phys. Rev. B*, 1995, **51**, 547-552.

17. F. Girgsdies and R. Schöllhorn, *Solid State Communications*, 1994, **91**, 111-112.

18. A. Nemudry, P. Rudolf and R. Schöllhorn, *Solid State Ionics*, 1998, **109**, 213-222.

19. A. Perrichon, A. Piovano, M. Boehm, M. Zbiri, M. Johnson, H. Schober, M. Ceretti and W. Paulus, *Journal of Physical Chemistry C*, 2015, **119**, 1557-1564.

20. A. Piovano, A. Perrichon, M. Boehm, M. R. Johnson and W. Paulus, *Physical Chemistry Chemical Physics*, 2016, **18**, 17398-17403.

21. A. Villesuzanne, W. Paulus, A. Cousson, S. Hosoya, L. Le Dreau, O. Hernandez, C. Prestipino, M. I. Houchati and J. Schefer, *J. Solid State Electrochem.*, 2011, **15**, 357-366.

22. M. Yashima, N. Sirikanda and T. Ishihara, *Journal of the American Chemical Society*, 2010, **132**, 2385-2392.

23. D. Parfitt, A. Chroneos, J. A. Kilner and R. W. Grimes, *Physical Chemistry Chemical Physics*, 2010, **12**, 6834-6836.

24. J.-M. Bassat, M. Burriel, O. Wahyudi, R. Castaing, M. Ceretti, P. Veber, I. Weill, A. Villesuzanne, J.-C. Grenier, W. Paulus and J. A. Kilner, *The Journal of Physical Chemistry C*, 2013, **117**, 26466-26472.

25. T. Ishihara, *J. Ceram. Soc. Jpn.*, 2014, **122**, 179-186.

26. M. Ceretti, O. Wahyudi, A. Cousson, A. Villesuzanne, M. Meven, B. Pedersen, J. M. Bassat and W. Paulus, *J. Mater. Chem. A*, 2015, **3**, 21140-21148.

27. O. Wahyudi, M. Ceretti, I. Weill, A. Cousson, F. Weill, M. Meven, M. Guerre, A. Villesuzanne, J. M. Bassat and W. Paulus, *CrystEngComm*, 2015, **17**, 6278-6285.

28. A. V. Kovalevsky, V. V. Kharton, A. A. Yaremchenko, Y. V. Pivak, E. V. Tsipis, S. O. Yakovlev, A. A. Markov, E. N. Naumovich and J. R. Frade, *J. Electroceram.*, 2007, **18**, 205-218.

29. K. Ishikawa, *Solid State Ionics*, 2014, **262**, 682-686.

30. M. Yashima, M. Enoki, T. Wakita, R. Ali, Y. Matsushita, F. Izumi and T. Ishihara, *Journal of the American Chemical Society*, 2008, **130**, 2762-2763.

31. L. Le Dréau, C. Prestipino, O. Hernandez, J. Schefer, G. Vaughan, S. Paofai, J. M. Perez-Mato, S. Hosoya and W. Paulus, *Inorg. Chem.*, 2012, **51**, 9789-9798.

32. V. Dyadkin, P. Pattison, V. Dmitriev and D. Chernyshov, *Journal of Synchrotron Radiation*, 2016, **23**, 825-829.

33. S. van Smaalen, *Incommensurate Crystallography*, Oxford University Press, 2007.

34. T. Janssen, G. Chapuis and M. de Boissieu, *Aperiodic Crystals From Modulated Phases to Quasicrystals: Structure and Properties*, Oxford University Press, 2018.

35. W. Paulus, H. Schober, S. Eibl, M. Johnson, T. Berthier, O. Hernandez, M. Ceretti, M. Plazanet, K. Conder and C. Lamberti, *Journal of the American Chemical Society*, 2008, **130**, 16080-16085.

36. M. I. Buckett, J. Strane, D. E. Luzzi, J. P. Zhang, B. W. Wessels and L. D. Marks, *Ultramicroscopy*, 1989, **29**, 217-227.

37. M. I. Buckett and L. D. Marks, *MRS Proceedings*, 1988, **129**, 521.

38. S. R. Maity, M. Ceretti, L. Keller, J. Schefer, T. Shang, E. Pomjakushina, M. Meven, D. Sheptyakov, A. Cervellino and W. Paulus, *Physical Review Materials*, 2019, **3**, 083604.

39. A. Bosak, D. Chernyshov, M. Hoesch, P. Piekarz, M. Le Tacon, M. Krisch, A. Kozłowski, A. M. Oleś and K. Parlinski, *Physical Review X*, 2014, **4**, 011040.

40. G. Campi, A. Bianconi, N. Poccia, G. Bianconi, L. Barba, G. Arrighetti, D. Innocenti, J. Karpinski, N. D. Zhigadlo, S. M. Kazakov, M. Burghammer, M. v. Zimmermann, M. Sprung and A. Ricci, *Nature*, 2015, **525**, 359.

41. J. M. Tranquada, D. J. Buttrey, V. Sachan and J. E. Lorenzo, *Phys. Rev. Lett.*, 1994, **73**, 1003-1006.

42. I. Berent and E. Polturak, *J. Low Temp. Phys.*, 1998, **112**, 337-354.

43. W. Petry, A. Heiming, J. Trampenau, M. Alba, C. Herzig, H. R. Schober and G. Vogl, *Phys. Rev. B*, 1991, **43**, 10933-10947.

44. M. A. Krivoglaz, *Diffuse Scattering of X-Rays and Neutrons by Fluctuations*, Springer-Verlag Berlin Heidelberg, 1996.

45. M. Mezger, H. Reichert, I. B. Ramsteiner, A. Udyansky, O. Shchyglo, V. N. Bugaev, H. Dosch and V. Honkimäki, *Phys. Rev. B*, 2006, **73**, 184206.

Supplementary Materials for

Long-range oxygen ordering linked to topotactic oxygen release in $Pr_2NiO_{4+\delta}$ fuel cell cathode material

Rajesh Dutta, Avishek Maity, Anna Marsicano, Monica Ceretti, Dmitry Chernyshov, Alexeï Bosak, Antoine Villesuzanne, Georg Roth, Giuditta Perversi, Werner Paulus[1]

Correspondence to: werner.paulus@umontpellier.fr

This PDF file includes:

Figs. S1 to S7

Table S1

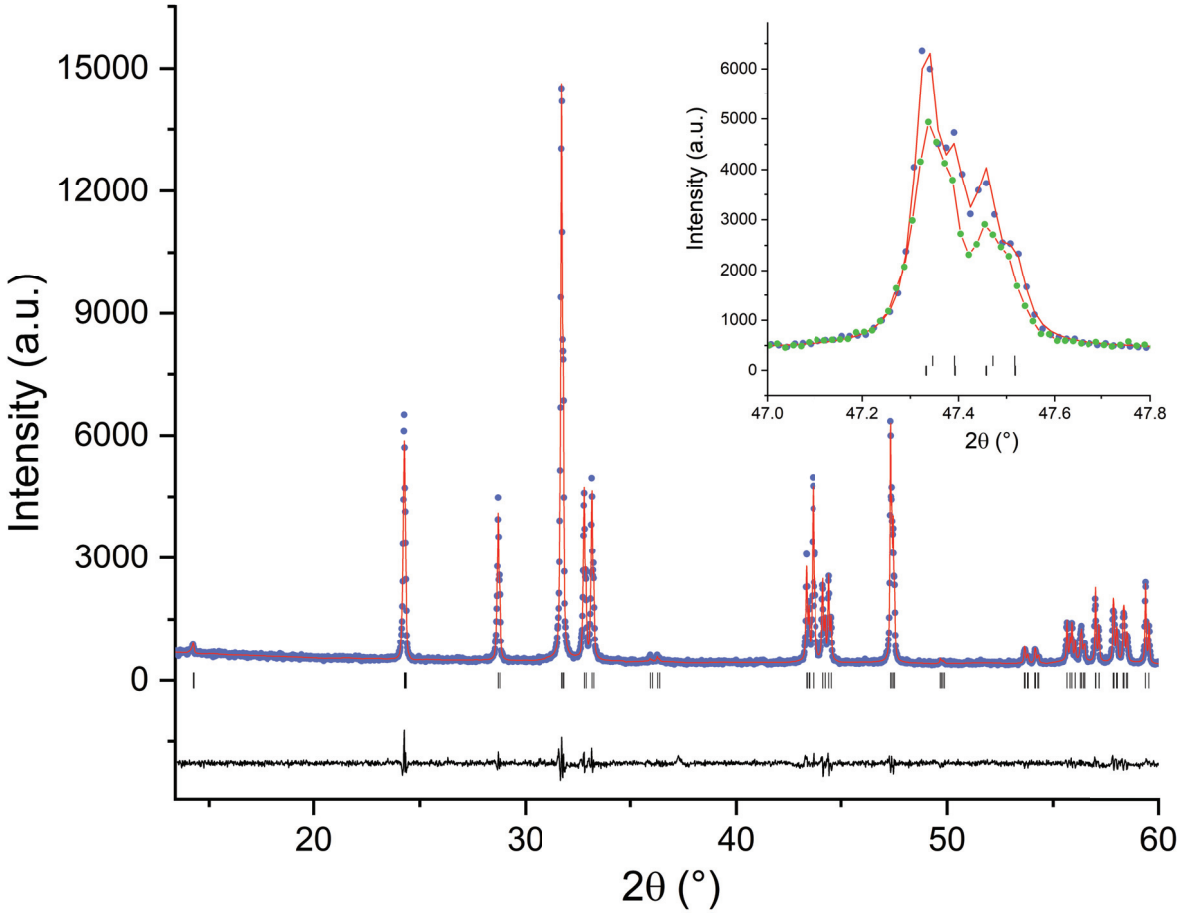

Fig. S1.

X-ray diffraction patterns of $Pr_2NiO_{4.225}$ (red line/light blue points) and $Pr_2NiO_{4.25}$ (inset only, all green), showing a monoclinic symmetry due to the splitting of the (220) reflections (see inset). XRD measurements were performed with a PANalytical X'Pert powder diffractometer (Cu $K_{\alpha1,2}$).

The very similar lattice parameter for both phases were refined in the F112/m space group.

$Pr_2NiO_{4.225}$: a = 5.3945(4) Å, b = 5.4538(4) Å, c = 12.4408(10)Å, γ = 90.07(1)°),

$Pr_2NiO_{4.25}$: a = 5.3977(3) Å, b = 5.4540(3) Å, c = 12.4362(10) Å, γ = 90.03°(1)

Due to the small monoclinic deviation a proper assignment of the true symmetry becomes difficult with laboratory powder diffraction.

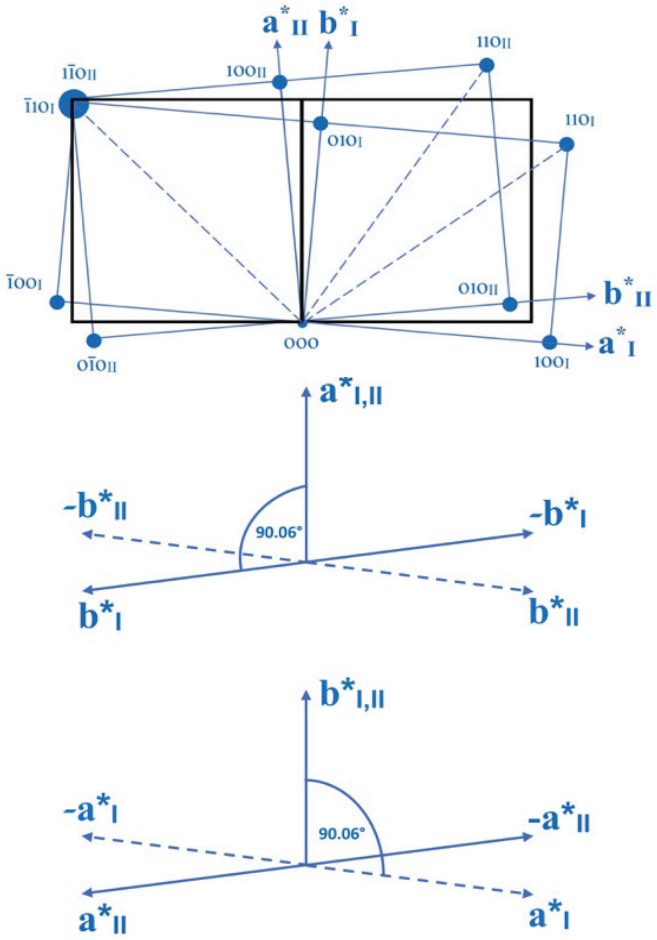

Fig S2: *(100)- and (010)-twinning scheme for a monoclinic lattice, the small deviation from 90° is graphically exaggerated. In reality, an almost perfect overlap of* (hkl) *and* $(h\bar{k}\bar{l})$ *reflections is achieved in the upper case, while for the lower figure this is true for couples of* (hkl) *and* $(\bar{h}k\bar{l})$ *reflections, the c-axis being the monoclinic axis. The loss of the mirror plane in the (a,c)- or (b,c)- plane of the orthorhombic phase, is then at the origin of the creation of the common plane for the monoclinic twin individuals. The proximity of the monoclinic angle to 90° renders this type of twinning to be taken as merohedral. Since* $(\bar{h}k\bar{l})$ *and* $(h\bar{k}\bar{l})$ *in a setting with a monoclinic c-axis are not equivalent by symmetry, both twin configurations finally deliver for this type of merohedry a different structure factor for overlapping reflections. In addition, it is difficult to determine the volume fraction of the respective two twin individuals. Both arguments taken separated or together, result in the important consequence to not allow to separate related superimposed intensities of the superstructure reflections, since there is always an almost perfect superposition of pairs of non-equivalent* (hkl) *and* $(\bar{h}k\bar{l})$ *in case of (010)-twinning as well as* (hkl) *and* $(h\bar{k}\bar{l})$ *reflections for (100)-twinning, rendering difficult further structure analysis beyond an average structure model. The given twinning scheme yields for each orthorhombic twin domain a maximum of 4 monoclinic twin domains, which could then result, in the presence of 4 orthorhombic twin domains, to a total number of 16 monoclinic domains. In case of a non-centrosymmetric space group this number would get even increased to 32. A macroscopic consequence of the twinning is the "appearance" of a second orientation of each incommensurate diffraction vector, resulting from the common (a,c) and/or (b,c) twin-planes and which corresponds in its orientation as being "mirrored" at these respective planes.*

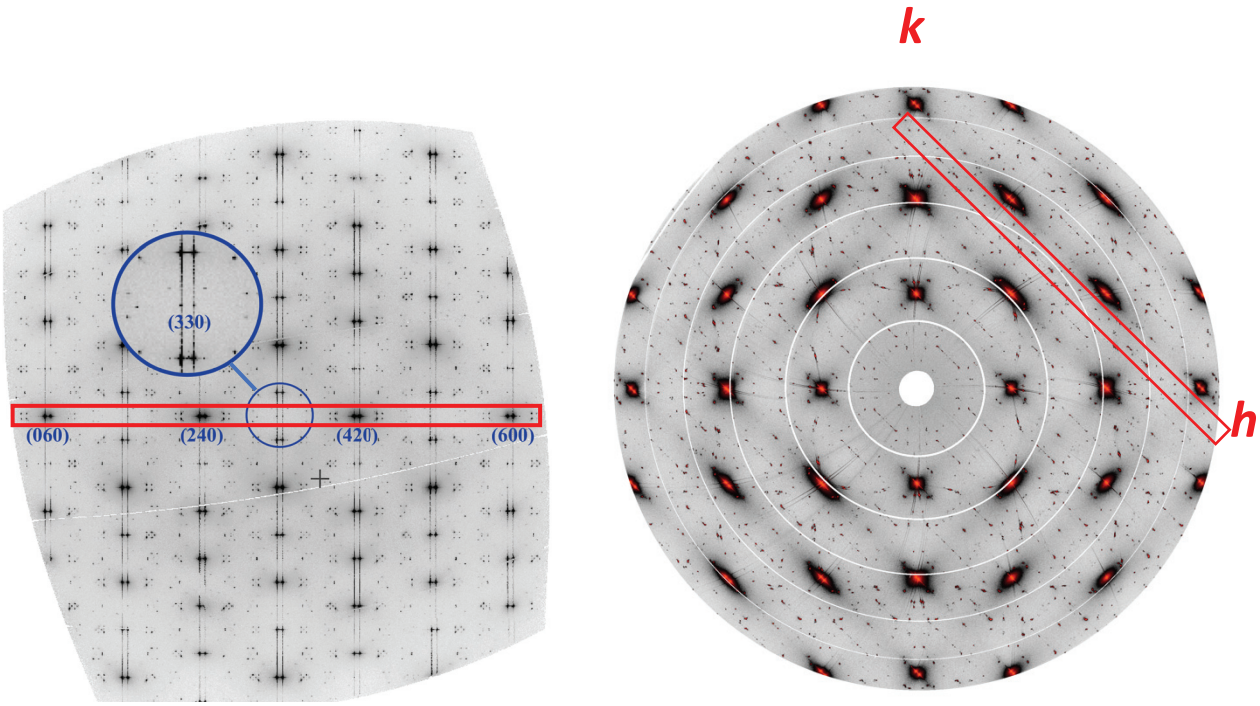

Fig. S3.

Left*: Section of the reciprocal lattice from (600) to (060) in the (a,b)-plane, with [001] vertical. The plane thus corresponds to a vertical cut of the (hk0)-plane as indicated in the right figure by the red box.*
Diffuse rods along the c-axis become evident, directly crossing reflections violating F-symmetry as for the (330). While the intensity of these "P-type"-reflections is essentially constituted by the diffuse intensity, there is also a significant contribution on the expected P-type reflection position as outlined in the zoomed region (large blue circle) around the (330) reflection (small blue circle).

Reconstructed (hk1) diffraction planes @ RT for $Pr_2NiO_{4+\delta}$

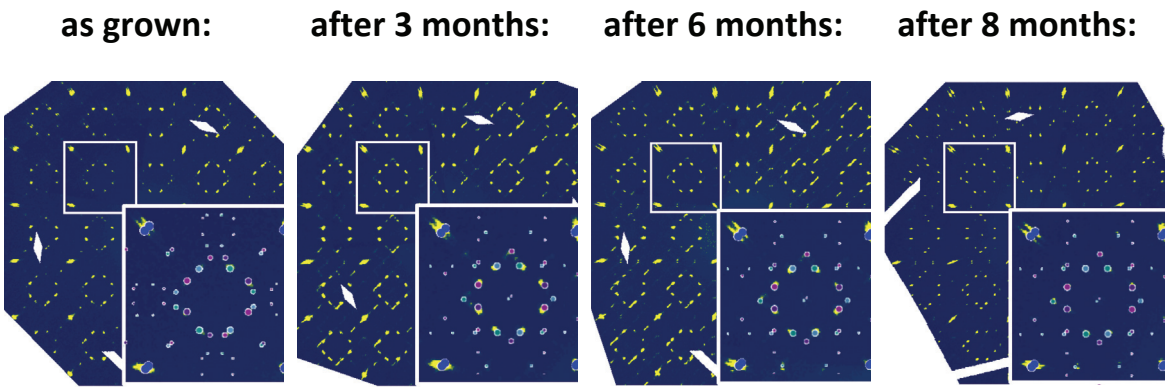

Simulated (hk1) diffraction planes @ RT for $Pr_2NiO_{4+\delta}$

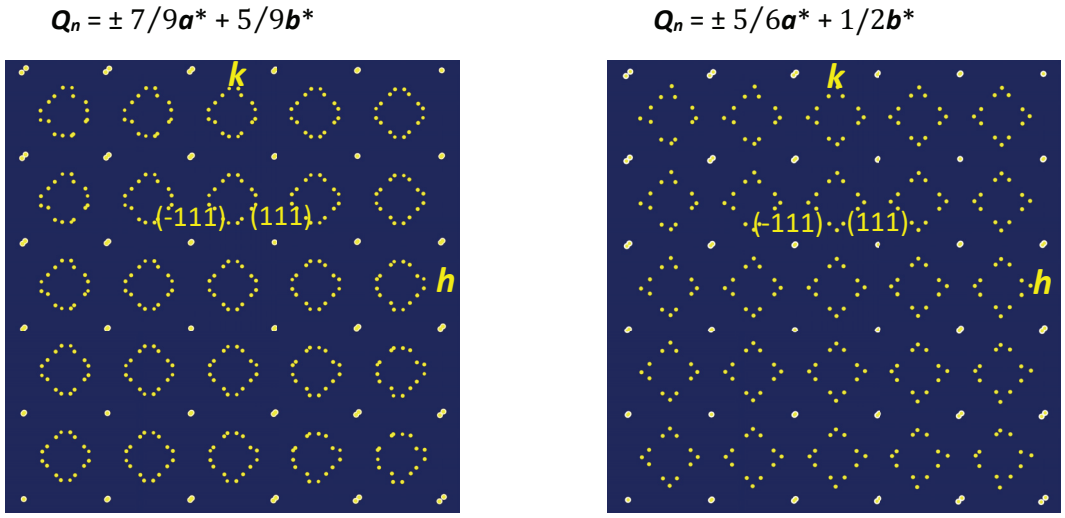

Fig. S4.

Top: *(hk1)-diffraction planes obtained on a STADIVARI diffractometer, equipped with a Mo μ-focus tube and 2K Pilatus detector for the as grown $Pr_2NiO_{4.25}$ (left) crystal, and after 3, 6, and 8 months, while reaching the final phase corresponding to $Pr_2NiO_{4.225}$. The starting phase $Pr_2NiO_{4.25}$ shows a modulation vector of $\boldsymbol{Q_n} = \pm 7/9\boldsymbol{a}^* + 5/9\boldsymbol{b}^*$ while the end phase $Pr_2NiO_{4.225}$ is characterized by a vector of $\boldsymbol{Q_n} = \pm 5/6\boldsymbol{a}^* + 1/2\boldsymbol{b}^*$. The zoomed square of the as grown crystal is overlaid with the simulated positions of $\boldsymbol{Q_n} = \pm 7/9\boldsymbol{a}^* + 5/9\boldsymbol{b}^*$, while for all other patterns the simulated positions correspond to $\boldsymbol{Q_n} = \pm 5/6\boldsymbol{a}^* + 1/2\boldsymbol{b}^*$. For the figures after 3 and 6 months we can clearly see the progressive evolution of the satellite positions towards the $Pr_2NiO_{4.225}$ final phase following a two phase reaction mechanism. A two-fold orthorhombic twinning with 4 monoclinic twin domains around [010]is taken into account for the simulations. The experimental data are overlayed with the simulated reflection positions while different colours account for different twin domains.*

Bottom: *Simulated (hk1)-planes for the different commensurate modulation vectors of the starting and final-reaction product after oxygen release, taking into account a maximum order for the satellites of m = 2, for simplification. This corresponds to what is essentially obtained from the diffraction data given in top of the figure. Higher order reflections are experimentally observed, but with very weak intensity only. For this reason, they are omitted here in the simulations.*

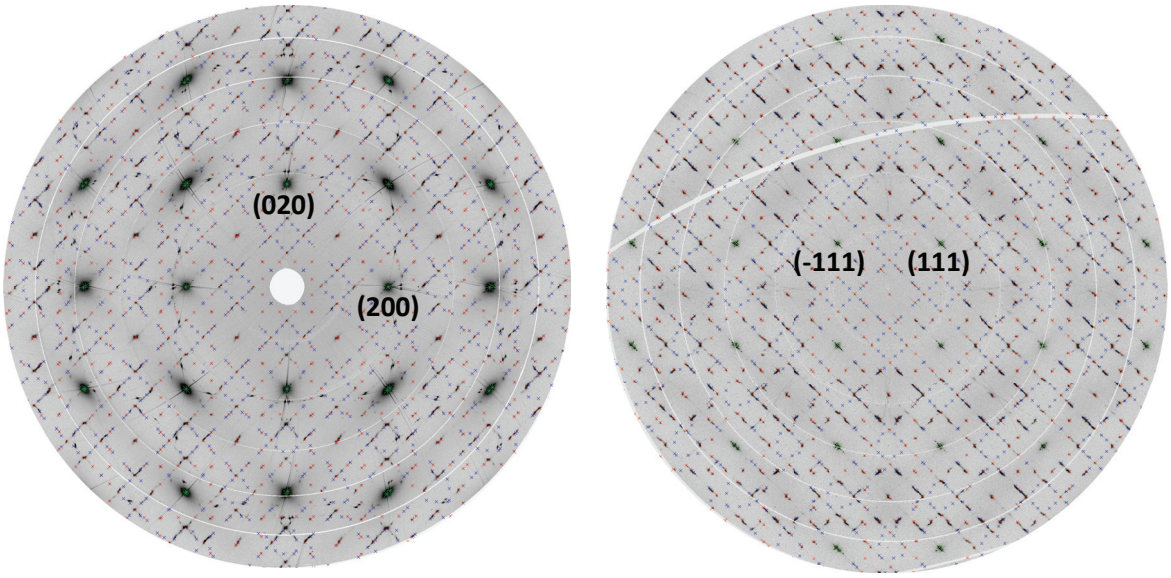

Fig. S5.
Reconstructed *(hk0)* and *(hk1)*-plane of $Pr_2NiO_{4.225}$, obtained on ID29@ESRF at RT. Green crosses correspond to the basic reflections, while red and blue crosses indicate respectively the satellite reflections of the $Pr_2NiO_{4.225}$ (modulation vector $Q_n = \pm 5/6a^* + 1/2b^*$ and a small contamination of $Pr_2NiO_{4.25}$ phase (modulation vector $Q_n = \pm 7/9a^* + 5/9b^*$), both phases simulated up to 5^{th} order). The contamination of the $Q_n = \pm 7/9a^* + 5/9b^*$ satellite reflections for the $Pr_2NiO_{4.225}$ phase is related to a not entirely finalized oxygen release, still containing a minor fraction of the as-grown $Pr_2NiO_{4.25}$ starting crystal.

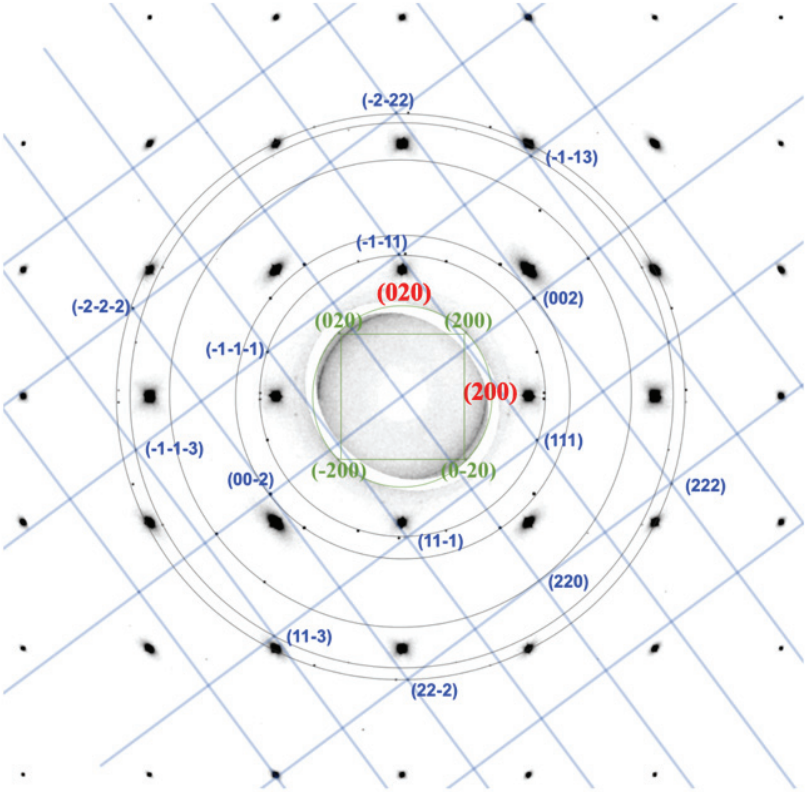

Fig. S6.

Reconstructed (hk0)-plane of $Pr_2NiO_{4+\delta}$ obtained from diffraction data on BM01 @ 700°C, (hkl) indexation given in red). This temperature is 800°C and thus 335°C above the monoclinic/tetragonal phase transition at 365°C, so no superstructure reflections related to oxygen ordering are observed any more. The additional reflections are related to a small amount of NiO, which is present as an intergrowth phase following NiO segregation as discussed in [ref. 1]. Totally four domains can be identified, which are twinned around [110], indexation is given in blue for one twin domain out of four. Debye-Scherrer lines of the (111), (200), (220), (113) and (222) are outlined to better visualize the equivalence by the same scattering angle, all given in blue.

Interestingly there are a few smaller spots with a higher d-value than the (111)-reflection (green), which correspond by their scattering angle and orientation to Ni_3O_4, showing a lattice parameter of 8.20Å, which has so far only been described following irradiation damage of NiO as given in [ref 2-3]. Ni_3O_4 is epitaxially grown on $Pr_2NiO_{4+\delta}$ with $[100]_{Ni3O4}$ parallel to the $[110]_{PNO}$, due to their similar d-values: $d_{(200)}Ni_3O_4$ = 4.1 Å, $d_{(220)}$PNO = 3.88Å, resulting into a lattice mismatch of about 5%.

[1] *Wahyudi, O. et al. Growth of high quality single crystals of strontium doped (Nd,Pr)-nickelates, $Nd_{2-x}Sr_xNiO_{4+\delta}$ and $Pr_{2-x}Sr_xNiO_{4+\delta}$, Crystengcomm **17**, 6278-6285, doi:10.1039/c5ce00906e (2015)*

[2] *Buckett, M., & Marks, L. (1988). Formation of a Ni_3O_4 Spinel Phase on the Surface of NiO During Electron Irradiation. MRS Proceedings, 129, 521. doi:10.1557/PROC-129-521*

[3] *M.I. BUCKETT, et al. Electron Irradiation Damage in Oxides, Ultramicrocopy, 29 (1989), 217-227*

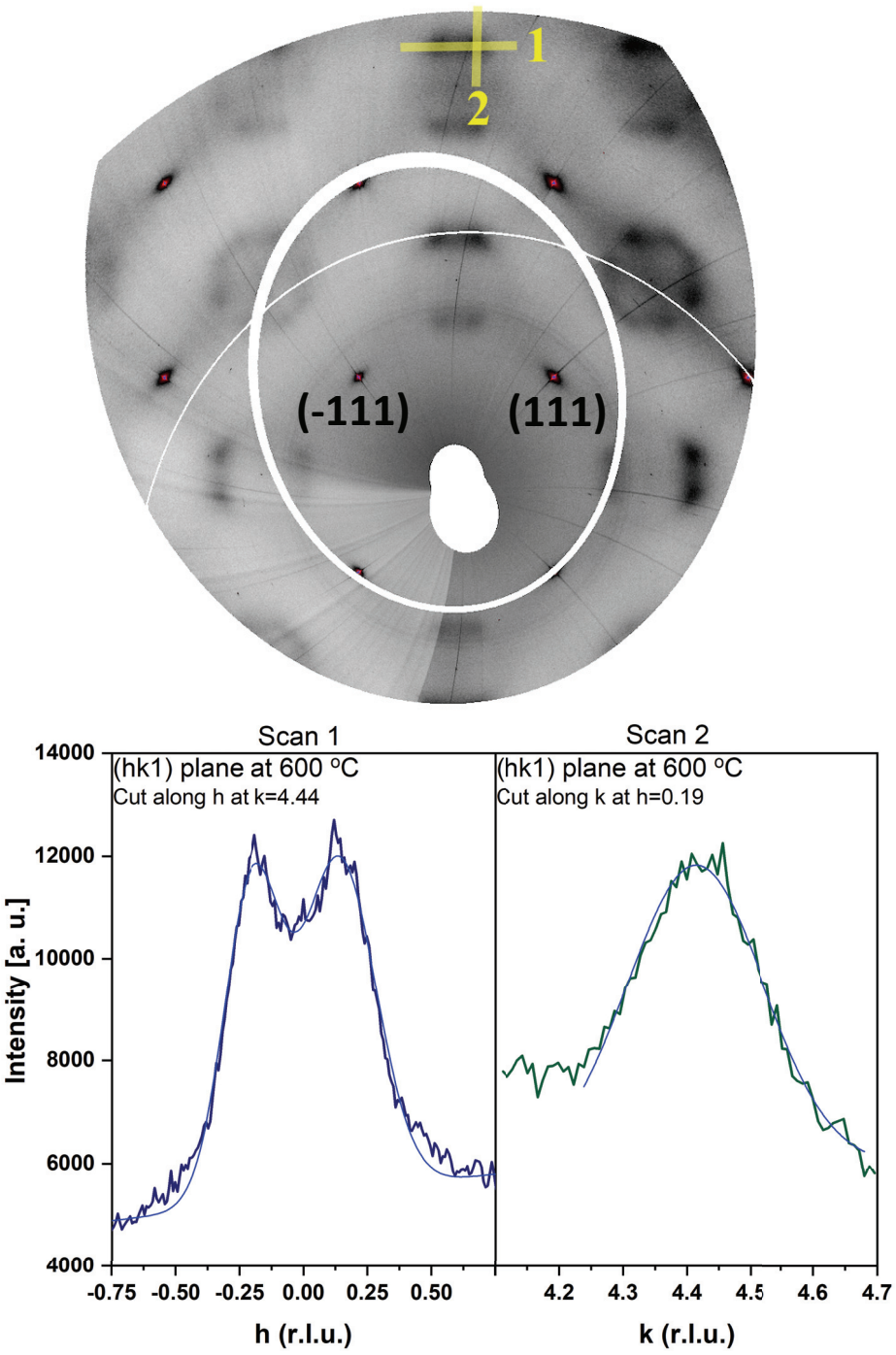

Fig. S7.

Diffuse scattering observed for $Pr_2NiO_{4.25}$ at 600°C. The line profiles indicated for different scan directions are outlined. Correlation lengths become difficult to interpret for double peak structures; we thus considered the "correlation range" as the inverse of the FWHM of the diffuse part under scan 2, which for Gaussian profiles are closely linked by their inversion, yielding 25 Å for the inverse FWHM.

Table S1.

Beamline specifications:

	BM01	**ID23**	**MX - ID29**	**ID28 side station**	**STOE STADIVARI laboratory diffractometer**
Wavelength	0.66305 A	0.688801 A	0.7 A	0.7 A	Microfocus source (Mo) 0.7107 Å
Beam size	~ 70 x 70 μm^2	50µm	50µm	20 x 40 μm^2	~ 150 µm
Detector distance from sample	142 mm	199 mm for RT and 400 mm for LT	250 mm	327 mm	50 mm
Monochromator	Double-crystal Si (111)	Si (111)	Si(111)	C(311)/Si(422)	X-ray fibre optics
Threshold Energy	8997 eV	10800 eV	10627 eV	18000 eV	12000 eV
Exposure time	0.5 s	0.053 s	0.25 s	0.2 s	30 s
Detector	DECTRIS PILATUS 2M (type – pixel, 172 x 172 μm^2)	DECTRIS PILATUS 6M (type – pixel, 172 x 172 μm^2)	DECTRIS PILATUS 6M-F (type – pixel, 172 x 172 μm^2)	DECTRIS PILATUS 1M (type – pixel, 172 x 172 μm^2)	DECTRIS PILATUS 200K (type – pixel, 172 x 172 μm^2)